Full-potential theoretical investigations of electron inelastic mean free paths and extended x-ray absorption fine structure in molybdenum

2014 J. Phys.: Condens. Matter 26 145401

(http://iopscience.iop.org/0953-8984/26/14/145401)

IOP Publishing Journal of Physics: Condensed Matter
J. Phys.: Condens. Matter **26** (2014) 145401 (8pp) doi:10.1088/0953-8984/26/14/145401

Full-potential theoretical investigations of electron inelastic mean free paths and extended x-ray absorption fine structure in molybdenum

C T Chantler and J D Bourke

School of Physics, University of Melbourne, Parkville, Vic, 3010 Australia

Email: chantler@unimelb.edu.au

Received 19 December 2013, revised 18 February 2014
Accepted for publication 19 February 2014
Published 20 March 2014

Abstract

X-ray absorption fine structure (XAFS) spectroscopy is one of the most robust, adaptable, and widely used structural analysis tools available for a range of material classes from bulk solids to aqueous solutions and active catalytic structures. Recent developments in XAFS theory have enabled high-accuracy calculations of spectra over an extended energy range using full-potential cluster modelling, and have demonstrated particular sensitivity in XAFS to a fundamental electron transport property—the electron inelastic mean free path (IMFP). We develop electron IMFP theory using a unique hybrid model that simultaneously incorporates second-order excitation losses, while precisely accounting for optical transitions dictated by the complex band structure of the solid. These advances are coupled with improved XAFS modelling to determine wide energy-range absorption spectra for molybdenum. This represents a critical test case of the theory, as measurements of molybdenum K-edge XAFS represent the most accurate determinations of XAFS spectra for any material. We find that we are able to reproduce an extended range of oscillatory structure in the absorption spectrum, and demonstrate a first-time theoretical determination of the absorption coefficient of molybdenum over the entire extended XAFS range utilizing a full-potential cluster model.

Keywords: electron energy loss function, inelastic mean free paths, x-ray absorption fine structure, x-ray spectroscopy

(Some figures may appear in colour only in the online journal)

1. Introduction

X-ray absorption fine structure (XAFS) analysis is a powerful experimental technique for non-invasive structural determinations of materials using synchrotron radiation. The XAFS phenomenon is observed as a series of oscillatory structures in the energy-dependent absorption spectrum of a material immediately following an ionization edge. These structures are the result of interference of the photoelectron wavefunction emitted by the ionization process, which interacts with neighbouring atoms within a small region in the absorbing material. In this way the photoelectron acts as a direct probe of local crystal structure, producing spectra sensitive to a range of material properties including bond lengths, co-ordination numbers, thermal disorder, static disorder, and inelastic scattering properties.

XAFS analysis is consequently widely used to fingerprint materials and to discriminate between possible local structure arrangements. XAFS measurements have also been used to measure Debye–Waller thermal disorder parameters, and recently have been demonstrated as an effective technique for measuring electron inelastic mean free paths (IMFPs) [1]. In order to maximize information content and absolute accuracy, all of these applications demand not only highly meticulous experimental arrangements, but also robust *ab initio* theoretical modelling.

This work focuses on advanced full-potential cluster modelling of XAFS, with particular emphasis on long energy-range calculations. The applicability of such an approach has only recently been demonstrated for metallic copper, a study which represented the first full-potential cluster computation of an entire XAFS spectrum [2]. This followed work demonstrating that accurate determination of the photoelectron IMFP is one of the most important considerations for maximizing agreement with experiment in the information-rich near-edge (XANES) region of the absorption spectrum [3].

We present here an improved theoretical model of inelastic electron scattering utilizing a many-pole dielectric theory incorporating both Lindhard [4] and Mermin [5] type functions to describe the dielectric response function of the scattering material. This enables a calculation that is inclusive of second-order excitation (e.g. plasmon) broadening, coupled for the first time with a precise representation of band structure effects in order to produce highly accurate IMFPs.

These developments are applied to elemental molybdenum in order to produce an accurate, physical, and robust determination of the x-ray absorption spectrum over the entire XAFS range and beyond—spanning up to 1.5 keV from the K-edge. This represents the most critical test of the theory currently available, in light of the exceptionally high absolute accuracy with which molybdenum XAFS have been measured [6]. These measurements were performed using the x-ray extended range technique, a method routinely demonstrated as providing uncertainties more than an order of magnitude lower than conventional XAFS measurements [7].

2. The electron inelastic mean free path

2.1 Theory

We focus firstly on the theory of the electron IMFP, which is most commonly expressed in terms of the complex dielectric function of the absorbing material, $\epsilon(q, \omega)$, following

$$\lambda(E)^{-1} = \frac{\hbar}{a_o \pi E} \int_0^{\frac{E-E_F}{\hbar}} \int_{q_-}^{q_+} \frac{1}{q} \mathrm{Im}\left[\frac{-1}{\epsilon(q,\omega)}\right] dq d\omega, \quad (1)$$

where, upon scattering, the electron deposits energy $\hbar\omega$ and momentum $\hbar q$ into the scattering material, and the limits of the momentum integral are given kinematically by

$$q\pm = \sqrt{\frac{2mE}{\hbar^2}} \pm \sqrt{\frac{2m}{\hbar^2}(E-\hbar\omega)}. \quad (2)$$

The terms a_0 and m are the Bohr radius and electron mass, while the Fermi energy, E_F, is defined relative to the bottom of the conduction band. The term $\mathrm{Im}[(-1)/\epsilon(q, \omega)]$ is referred to as the electron energy loss function (ELF), and can be interpreted as a relative probability of scattering with a particular energy and momentum transfer (q, ω). This quantity, or equivalently the dielectric function $\epsilon(q, \omega) = \epsilon_1(q, \omega) + i\epsilon_2(q, \omega)$, is the principal determinant of the IMFP.

The electron ELF is difficult to calculate directly, and is most commonly obtained via some variation of the optical data model of Penn [8]. This model utilizes a determination of ELF in the optical limit, i.e. where $q \to 0$, followed by an extension algorithm to obtain the function at finite values of q following the expected dispersion relation of plasmon and other electronic excitations. In this work, we implement for the first time a version of this technique that includes a full lifetime-dependent representation of plasmon excitations, in addition to a precise reproduction of an *ab initio* calculation of the optical ELF from density functional theory (DFT).

The first component of this calculation-the optical ELF-is evaluated using the band structure package WIEN2k [9]. This package invokes a self-consistent field algorithm to solve the Kohn–Sham equation describing the electronic potential and eigenstates in a periodic condensed matter system. These eigenstates can then be used to calculate a complete set of momentum matrix elements describing optical transition probabilities in the dipole approximation, following

$$M_{n',n}(k, q) = \left\langle n', k \left| e^{-iq.r} \right| n, k+q \right\rangle. \quad (3)$$

The matrix elements define uniquely the electronic response of the condensed matter system to photon perturbations, and so can be used to express the optical dielectric function $\epsilon(0, \omega)$. Specifically, following [10], they provide a modulation to the Lindhard dielectric function, describing the response of a homogeneous gas of charge [4]:

$$\epsilon(0,\omega) = 1 + \lim_{q\to 0} \frac{4\pi e^2}{q^2} \times \sum_{n,n',k} \frac{f^0(k) - f^0(k+q)}{E(k+q) - E(k) - \hbar\omega} \left| M_{n,n'}(k,q) \right|^2 \quad (4)$$

where $f^0(k)$ is the Fermi distribution. This enables a direct theoretical determination of the optical ELF $\mathrm{Im}[(-1)/\epsilon(0, \omega)]$ from DFT [11]. Following this, we must then extend the optical ELF to a full momentum-dependent ELF according the expected dispersion relation of plasmon excitations.

This task has been undertaken by a number of authors using slightly different variations of optical data modelling, involving classical or empirical plasmon functions based on Drude–Lorentz theory [12, 13], lossless partial plasmon poles based on Lindhard theory [14, 15], or unconstrained lifetime-dependent many-pole models based on Mermin theory [16, 17]. Here we undertake for the first time a hybrid approach utilizing both Mermin and Lindhard components in order to produce a constrained loss spectrum in the optical limit, coupled with lifetime broadening at increased values of momentum transfer $\hbar q$.

To do this we must clearly define both the Lindhard and Mermin theories of plasmon excitations and their relationship to one another. While equation (4) is a direct statement describing the dielectric behaviour of modulated plasmons under the Lindhard theory, it is useful to express the Lindhard dielectric function in a more direct way following [4]

$$\epsilon_L(q, \omega) = 1 + \frac{3\omega_p^2}{q^2 v_F^2} f, \quad (5)$$

where

$$f = \frac{1}{2} + \frac{1}{8z}[1-(z-u)^2]\ln\left[\frac{z-u+1}{z-u-1}\right] + \frac{1}{8z}[1-(z+u)^2]\ln\left[\frac{z+u+1}{z+u-1}\right]. \quad (6)$$

This is expressed in term of dimensionless parameters z and u, which are given by

$$u = \frac{\omega}{q v_F}, \quad (7)$$

$$z = \frac{q}{2q_F}. \quad (8)$$

The v_F and q_F terms are the Fermi velocity and momentum, respectively. Although this formulation is mathematically complex, the most important aspect of the Lindhard theory to this discussion is that although it is well defined for a quantized gas of charge, it does not include any account of lifetime broadening, or second-order energy loss due to the inelastic scattering of plasmons. This can be convenient in a sense, because it gives rise to a collection of delta functions in the optical ELF, which can be summed with appropriate amplitude parameters in order to completely reproduce any optical ELF determined via DFT [18]. In this way, one can readily build a momentum-dependent electron ELF following the natural q-dependence of the Lindhard function, which also perfectly replicates the result from DFT at $q = 0$. Specifically, one can write

$$\mathrm{Im}\left[\frac{-1}{\epsilon(q,\omega)}\right] = \sum_i A_i \mathrm{Im}\left[\frac{-1}{\epsilon_L(q,\omega)}\right], \quad (9)$$

where

$$\sum_i A_i \mathrm{Im}\left[\frac{-1}{\epsilon_L(0,\omega)}\right] = \mathrm{Im}\left[\frac{-1}{\epsilon_{DFT}(0,\omega)}\right]. \quad (10)$$

However, such an approach is also unphysical. The problem of implementation of lifetime broadening into the Lindhard theory is solved by the alternative use of the Mermin dielectric function, which can be written in terms of the Lindhard function following [5]

$$\epsilon_M(q,\omega) = 1 + \frac{(1+i\gamma/\omega)[\epsilon_L(q,\omega+i\gamma)-1]}{1+(i\gamma/\omega)[\epsilon_L(q,\omega+i\gamma)-1]/[\epsilon_L(q,0)-1]}, \quad (11)$$

where γ is now a broadening parameter associated with a plasmon lifetime $\tau = 1/\gamma$. The Mermin function has several elegant properties, including reducing to the Lindhard expression for $\gamma \to 0$, reducing to the classical Drude theory for $q \to 0$, and satisfying optical sum rules (specifically, Kramers–Kronig and f-sum rules) [19] for all values of γ. The implementation of Mermin terms instead of Lindhard terms represents an improved physical modelling of plasmon excitations, however it comes at the cost of uniqueness. Due to the ability to choose values of both excitation amplitudes and broadening terms, it is possible to approximately reproduce optical loss data from DFT (or other sources) using a number of different parameter sets. Further, the use of Mermin terms typically means that the optical ELF is not reproduced in the precise manner that is possible when using Lindhard terms.

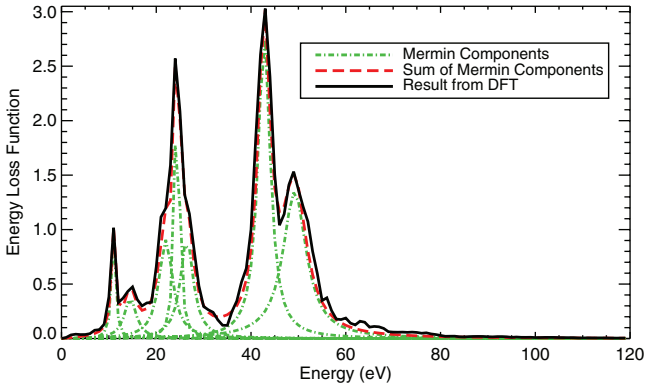

Figure 1. Optical ELF for molybdenum, calculated using density functional theory (solid black line), along with a Mermin fit to the spectrum (dashed red). Dot–dashed green curves correspond to individual Mermin components, representing assigned plasmon resonances.

2.2 Results

The problem of ambiguity in the Mermin parametrization can only be alleviated through careful consideration of the major peaks visible in the optical loss spectrum, and ultimately this results in a small but inevitable variability in the theory. The problem of imprecise matching to optical ELF data, however, can be solved entirely by utilizing a hybrid approach with both Mermin and Lindhard type terms. In figure 1 we illustrate the optical ELF for molybdenum, determined via DFT (solid black curve), along with a collection of seven Mermin functions approximating the electronic excitations that make up the spectrum (dot–dashed green curves). The sum of the Mermin functions is also shown (dashed red curve).

This representation is quite effective in reproducing the optical ELF, covering more than 90% of the losses with only a few discrete components. Typically when using the Mermin approach, authors will attempt to match the optical ELF as closely as possible in this fashion, and then follow an equivalent of equations (10) and (11) to produce the electron ELF and subsequent IMFP. By contrast, we implement a close fitting set of Mermin parameters that (where possible) do not exceed the total losses of the optical ELF from DFT, and account for superfluous losses via a Lindhard representation. Therefore, we can build the optical ELF as a sum of both Mermin and Lindhard parts, as shown in figure 2. This allows us to faithfully reproduce the DFT result without abandoning the implementation of plasmon lifetime broadening terms.

The Lindhard part of the spectrum (dot–dashed blue curve) includes the more detailed oscillations not readily represented with Mermin components, and likely to contribute little in terms of the broadening effect on the IMFP. A small area of the Lindhard part, comprising less than 1% of the total spectrum, is negative. This is designed to approximately negate

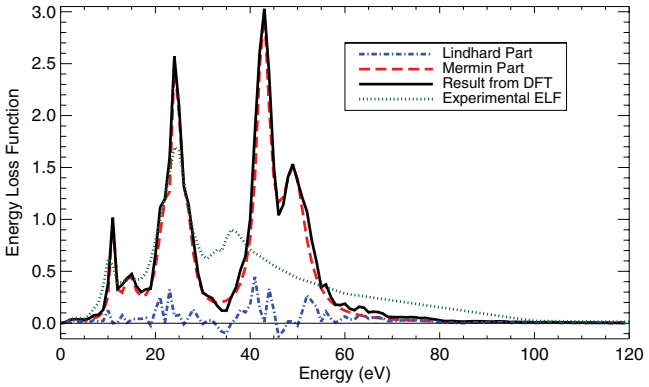

Figure 2. Optical ELF for molybdenum, showing a comparison between the result from DFT (solid black line) and the experimental tabulation of Palik (dotted green line) [20]. Also shown are the Mermin (dashed red) and Lindhard (dot–dashed blue) partitions used to build the optical ELF by fitting to the DFT result.

the effect of Mermin terms that implement higher losses than indicated by the DFT result. The uncertainty of this on the electron ELF is confidently estimated to be less than 0.2%.

Figure 2 also includes an optical ELF determined experimentally and reported in the oft-cited optical data compilation of Palik [20] (dotted green curve), which is commonly used for IMFP determinations with the optical data model [14]. This result is dramatically different from our DFT result. However, it is not unusual for a lack of consistency to be seen in experimental optical ELF data in this energy range [11]. We include this result to demonstrate the effect of not only a hybrid plasmon representation, but also of purely theoretical determinations of the optical spectrum on the resulting IMFP. A similar study on the effect of DFT on calculated IMFPs was recently conducted for copper, with the theoretical prediction leading to significant improvements observed [21].

The full electron ELF calculated for molybdenum is illustrated in figure 3 in terms of the Mermin (red surface) and Lindhard (blue mesh) parts. The evolution of peak energies as a function of momentum transfer is similar for both, however the Mermin part of the spectrum loses its distinctive shape far more rapidly than the Lindhard part.

The effect of the increased broadening apparent in the Mermin theory is that more of the loss spectrum remains in the low energy region as q is increased, leading to higher values of the integrand of equation (1) at low energies [18]. Accordingly, we expect the inclusion of Mermin broadening to lower the electron IMFP. Similarly, by comparison with the experimental optical ELF shown in figure 2, we expect the use of a DFT ELF to itself result in extra losses and hence, lower IMFP values in the energy range studied. In figure 4 we examine these considerations with a range of IMFP values determined from different approaches.

Firstly we show the IMFP resulting from use of a purely Lindhard type representation of the experimental optical ELF given by [20] (dotted green curve). We then apply the same approach to the optical ELF from DFT (dot–dashed blue curve), before finally including Mermin terms into our representation, as described (dashed red curve). Also shown for

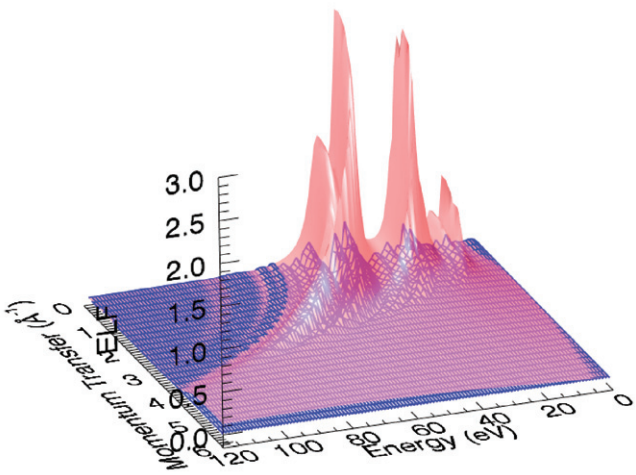

Figure 3. Electron ELF of molybdenum in terms of summed Mermin components (red surface) and summed Lindhard components (blue mesh). The evolution of the loss structure at higher momentum transfer is apparent, with the Mermin structure broadening and becoming less defined more quickly than that of the Lindhard structure. These curves are summed to produce the total electron ELF, which matches the optical ELF from DFT for $k = 0$, and can be integrated to find the inverse IMFP.

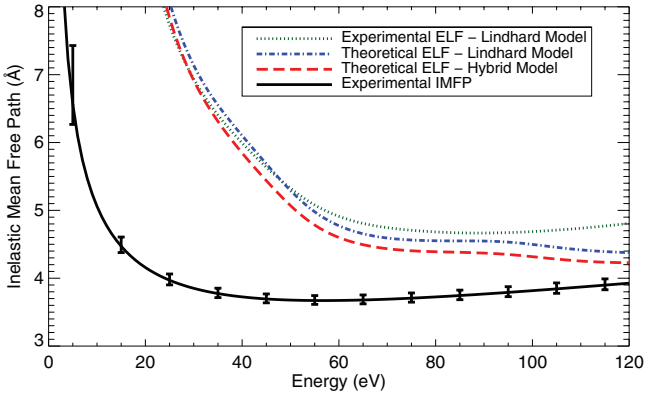

Figure 4. Electron IMFPS for molybdenum. The solid black curve is an experimental result produced using a fit to the solid-state (oscillatory) component of the measured XAFS spectrum [22]. The dotted green curve uses typical theory methods, involving a Lindhard extension to experimental optical data tabulated by Palik. The dot–dashed blue curve instead utilizes optical data from DFT with a Lindhard model, while the dashed red curve uses a hybrid model involving both Mermin and Lindhard components in the finite-q extension of the DFT ELF, as shown in figure 3.

comparison is a recent measurement of the electron IMFP for molybdenum determined via analysis of the XAFS measurements of de Jonge *et al* [22]. The experimental curve represents the IMFP values best used to achieve maximum agreement between XAFS theory and experiment, with respect to the oscillatory part of the absorption spectrum.

Figure 4 shows that the implementation of optical ELF data from DFT indeed results in a significant reduction in the IMFP beyond around 50 eV, and a very significant reduction after 100 eV. The effect arises somewhat higher in energy than the regions where the optical ELFs diverge, due to the dispersion relation observable in figure 3. At 120 eV, the difference between theory and experiment is roughly halved by the use

of DFT alone. A similar result has also been demonstrated recently for studies of the IMFP in copper [21].

The inclusion of plasmon broadening via a Mermin representation of the ELF also provides a significant contribution to a reduction in the IMFP. In this case the reduction is across all energies, and again at 120 eV the difference between theory and experiment is almost halved. Since the optical ELF of molybdenum is characterized by particularly tall, thin peaks, the effect of broadening terms would be greater still in many other materials where particularly broad loss spectra are seen; notable examples include silver [11], gold [16], and copper [18].

Given that the experimental IMFP of figure 4 represents the best possible values for agreement between XAFS theory and experiment, the improvement in agreement with theoretical IMFP values from the optical data modelling is strongly important for XAFS analysis. We now turn our attention to the specifics of XAFS modelling using the improved IMFP theory, coupled with advancements in finite-difference method cluster calculations.

3. X-ray absorption fine structure

3.1 Theory

Our calculations of XAFS are performed via implementation of an explicit finite-difference method modelling of the final-state wave function of an excited photoelectron in a small cluster. This is done chiefly through the package FDMNES (finite-difference method for near-edge structure) [23], however with a number of extensions and, in particular, a detailed additional implementation of recent developments in the theory of inelastic electron scattering as described.

FDMNES calculations treat the problem of XAFS in a relatively general way, starting from the basic need to determine the optical transition matrix elements which, in the quadrupolar approximation, may be written as

$$M_{gf} = \left\langle \psi_f \left| (1 + \frac{i}{2} k \cdot r) \right| \psi_g \right\rangle, \tag{12}$$

where $\boldsymbol{k}$ is the photon wave vector polarized in the $\boldsymbol{\epsilon}$ direction, and ψ_g and ψ_f are the initial and final states. The transition amplitudes are then summed to give the absorption cross section σ following

$$\sigma = 4\pi^2 \alpha \hbar\omega \sum_{f,g} \left| M_{gf} \right|^2 \delta(\hbar\omega - E_f + E_g), \tag{13}$$

where α is the fine structure constant, $\hbar\omega$ the energy of the incident photon, and E_f, E_g the final and initial state energies. The initial state is that of an electron bound to an atomic core orbital, and therefore relatively well known. It is the final state that is calculated using the FDM.

The FDM essentially solves a large number of simultaneous linear equations linking the values of the wave functions ψ_i, and potentials V_i, at points i in a defined grid in real space. The Laplacian operator needed to solve the Schrödinger equation is approximated using a fourth-order polynomial and may be written as [23]

$$\nabla^2 \psi_i = \frac{1}{h^2} \left(\frac{4}{3} \sum_{j,\epsilon} \psi_j^{\epsilon} - \frac{1}{12} \sum_{j,\epsilon} \psi_j^{\epsilon\epsilon} - \frac{15}{2} \psi_i \right). \tag{14}$$

Here $\epsilon = +$ or $-$, and ψ_j^{ϵ} and $\psi_j^{\epsilon\epsilon}$ are the first and second nearest neighbouring grid points to i in the direction ϵj. Particular note must be made that for this equation h is defined as the interpoint distance, or distance between adjacent grid points, and *not* Planck's constant. With this approximated Laplacian, the Schrödinger equation is expressed in discretized form, following [23], as

$$(-\nabla^2 + V_i - E)\psi_i + \sum_j \left(-\nabla^2 \psi_j \right) = 0, \tag{15}$$

where again ψ_j refers to wave function values at grid points neighbouring i. The values of the wave function can then be determined for all points i according to the potential values V_i. These potentials are determined via an independent atom approximation [24], utilizing the Coulomb potential produced by defined ground state electron densities plus the Hedin–Lundqvist exchange-correlation potential [25]. Although not inherently self-consistent, this approach is robust and widely applicable as, unlike with LAPW approaches, it does not require a periodic potential and so can be applied to nano materials and other small clusters.

The photoelectric absorption spectrum calculated via the FDMNES package must be obtained using very precise computational parameters, particularly with regards to cluster size and density, in order to yield accurate results at energies far beyond the near-edge region (i.e. $E \gg 100$ eV) [2]. In this work, the results are also subject to a post-processing routine to implement a range of additional physical processes including core-state lifetime broadening, thermal and structural disorder, outer orbital absorption, x-ray scattering, and inelastic photoelectron scattering [3]. The main focus of this work, the inelastic photoelectron scattering, appears in XAFS spectra as an energy-dependent Lorentzian convolution of width $\Gamma_\lambda(E)$, principally determined by the electron IMFP $\lambda(E)$:

$$\Gamma_\lambda(E) = \frac{\hbar}{\lambda(E)} \sqrt{\frac{2E}{m_e}} \tag{16}$$

3.2 Results

In figure 5 we show the mass attenuation coefficient for molybdenum calculated using the extended FDM procedure with implementation of inelastic photoelectron scattering via the described DFT/Mermin model of IMFPs (dashed red curve). In addition, we plot a version of the theory utilizing the fitted (experimental) values for the IMFP from figure 4 (solid black curve). The measurement of the mass attenuation coefficient (purple diamonds) is from the work of de Jonge *et al* [6], and possesses uncertainties of around 0.03% over much of the energy range of interest.

There exists a significant offset between the theoretical and experimental results, which is commonplace for absorption determinations close to ionization edges (e.g. [26–28]), and

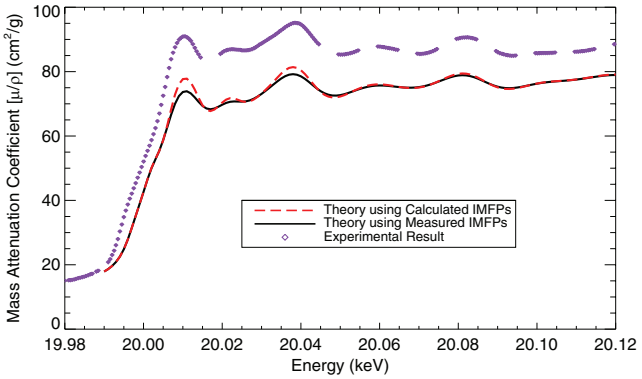

Figure 5. Mass attenuation coefficient of molybdenum near the K absorption edge, showing XAFS. Experimental data from de Jonge *et al* is given as purple diamonds [6]. Theoretical results are calculated using IMFPs from the hybrid Mermin/Lindhard model coupled with DFT (dashed red curve here and in figure 4) and using experimentally determined IMFPs (solid black curve here and in figure 4) [22].

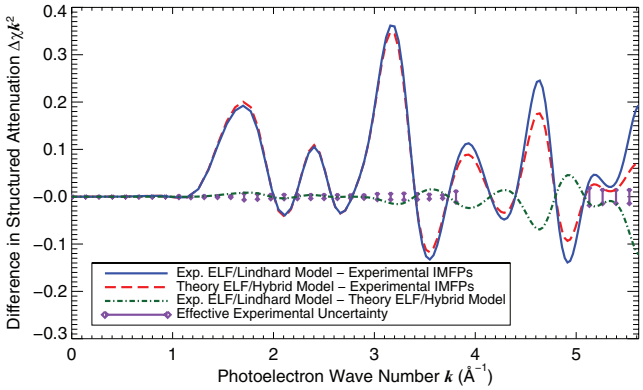

Figure 6. Triangular comparison of differences in the oscillatory part of the absorption spectrum, $\chi(k)$, for molybdenum XAFS using theoretical modelling with different values of the electron IMFP. The marked purple components reflect the relative level of uncertainty in the measured data of de Jonge *et al*, demonstrating the significance of these differences. In particular, we note that while little significance is observed at very low values of k, towards the end of our plotted range the effect of our refinements in IMFP determination (dot–dashed green curve) is seen to result in changes in the XAFS spectrum of several sigma.

has been shown using alternate XAFS modelling recently for solid molybdenum [29]. This problem is not currently well understood, but is sometimes artificially removed via the use of an empirical spline, with the knowledge that a smooth background function does not materially change conclusions regarding the information from XAFS.

The important aspect of our result is that the oscillatory structure has been quite well reproduced by the theoretical modelling. The black curve represents the most consistent result possible with experiment using ideal values for the electron IMFP, and so deviates somewhat from our result using DFT/Mermin theory at low energies. This is due to the significant differences in IMFPs in the low energy region, which we believe may be attributed to the absence of exchange and correlation effects in the Mermin dielectric theory (see, for example [21, 30]), or excitonic/electron screening effects [31]. Towards the higher end of the spectrum, these differences appear to be minor, and at first glance may seem insignificant.

Such an appearance can be misleading, however, as the oscillatory structure is the molybdenum absorption spectrum has been quantified to exceedingly high accuracy. In figure 6 we show the differences in attenuation predicted by theoretical modelling using the different IMFP values given in the previous section. For example the dot–dashed green curve shows the difference in the XAFS results from using either the Lindhard model coupled to Palik's compiled ELF data, or the Mermin model coupled to ELF data from DFT. The purple lines represent the relative level of uncertainty in the experimental measurements in this region. The abscissa is given in terms of the photoelectron wave number k following common practise in XAFS analysis literature, however the scale is, as before, bounded at 120 eV above the absorption edge.

This demonstrates that despite the relatively small magnitudes of deviation, the effect of changing the IMFP values within the theory is quite significant with respect to the experimental uncertainty. Further developments are clearly needed in the lower energy part of the spectrum, however we can see

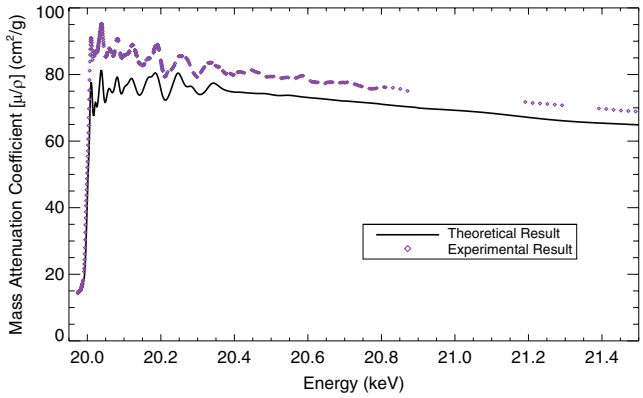

Figure 7. Mass attenuation coefficient of molybdenum, covering an energy range of 1.5 keV ($k \approx 20$) from the K absorption edge. Experimental results from de Jonge *et al* are shown as purple markers [6], while the black curve is calculated using full-potential cluster modelling. The jump-height offset diminishes rapidly over the first 400 eV, but stabilizes and remains present even into the smooth, atom-like absorption region.

that the improvements enabled by consideration of DFT-based optical data and a properly broadened electron ELF result in XAFS calculations that are more accurate by 2 to 5 σ for k values above 4 Å^{-1}, corresponding to around 50 eV.

We can extend our XAFS calculation to greater energies by utilizing other tabulations of IMFP data [14] which, while evaluated using the less physical Lindhard model, will converge to the Mermin result at sufficiently high energies [18]. Coupled with computational developments and the post-processing implementation of other physical effects as stated, it is possible to utilize the FDM to generate theoretical mass attenuation spectra over an energy range exceeding the visible region of XAFS. We demonstrate this outcome in figure 7, reporting for the first time in molybdenum a consistent theoretical determination of the entire XAFS spectrum utilizing a full-potential model.

We see that the oscillatory structure is qualitatively extremely well reproduced up to at least 400 eV above the absorption edge. This range is nearly an order of magnitude greater than the range of consideration typical for FDM type investigations of XAFS without the extension algorithms that we have implemented. The spectrum is extended up to 1.5 keV from the edge (corresponding to $k \approx 20$), and in the higher energy region we see that some small oscillations remain in the experimental result that are absent from the theory. We speculate that this problem may be partly the result of an insufficient level of sophistication in our treatment of atom-specific thermal parameters [3], and perhaps partly the result of convergence issues related to the size of the highly dense cluster modelling increasingly required at high photoelectron energies.

An interesting consideration separate from the XAFS analysis is the nature of the smooth offset between theory and experiment, which decays steadily for the first 400 eV, but thereafter reduces quite slowly, resulting in a lack of observed convergence between the atom-like spectra characteristic at energies well beyond the XAFS region. A previous study of copper using the FDM demonstrated convergence between theory and experiment around 400–500 eV above the absorption edge [2]. The physical nature of this offset is not well understood, but as stated he effect is common in XAFS analysis, resulting in the standard use of empirical splines rather than *ab initio* atomistic theories in order to extract the oscillatory components of measured XAFS spectra. Although we are unable to make specific conclusions about the nature of the effect simply from this result, we hope that by adding to the range of elements studied in this way that patterns may be observed that can light the way on this difficult and important problem.

4. Conclusions

We have demonstrated the significant improvement to the theory of inelastic electron scattering via the IMFP parameter obtained through explicit consideration of well constrained, self-consistent *ab initio* modelling of the optical energy loss function, coupled with physical modelling of second-order (plasmon) lifetime effects in the electronic ELF. These improvements have been shown to reduce the disparity between theory and experiment by up to 75% at critical energies relevant to precision XAFS investigations.

The importance of high-accuracy theoretical modelling of IMFPs has been demonstrated in terms of the direct significance in molybdenum, with improvements of several σ observed in the calculated XAFS spectrum as a direct result of our IMFP analysis. Further, calculations of mass attenuation coefficients for molybdenum using these and other developments have been demonstrated over an energy range of 1.5 keV from the K absorption edge, representing the most robust test yet of full-potential solid-state absorption theory.

These results confirm not only the validity and accuracy of the FDM approach, but provide further evidence of its versatility over a wide energy range encompassing all observable XAFS. They also directly add to a growing body of work demonstrating the long-energy range relationship between experimental and theoretical determinations of optical absorption—a fundamental area of investigation with strong need for additional data and analysis.

This work is directly applicable to a range of structural, chemical, and electronic investigations due to the versatility of both the XAFS technique and of the FDM modelling scheme. The use of a finite cluster allows consideration of nano materials, amorphous materials, catalytic centres or localized defects. The use of a full-potential model permits high accuracy for multi-elemental materials, particularly in the near-edge region, commonly unattainable by methods with approximated or unphysical potential arrangements. Our results and developments demonstrate the robust use of this approach for analysis of XAFS over an arbitrary energy range within a single consistent theoretical framework.

Acknowledgments

The authors acknowledge the work of Y Joly, Z Barnea, M D de Jonge, N A Rae and J L Glover, and their helpful contribution to the development of ideas important to this research.

References

[1] Bourke J D and Chantler C T 2010 *Phys. Rev. Lett.* **104** 206601
[2] Bourke J D and Chantler C T 2010 *Nucl. Instrum. Meth. Phys. Res.* A **619** 33
[3] Bourke J D, Chantler C T and Witte C 2007 *Phys. Lett.* A **360** 702
[4] Lindhard J 1954 *Dan. Vidensk. Selsk. Mat. Fys. Medd.* **28**
[5] Mermin N D 1970 *Phys. Rev.* B **1** 2362
[6] de Jonge M D, Tran C Q, Chantler C T, Barnea Z, Dhal B B, Cookson D J, Lee W and Mashayekhi A 2005 *Phys. Rev.* A **71** 032702
[7] Chantler C T 2009 *Eur. Phys. J. Spec. Top.* **169** 147
[8] Penn D R 1987 *Phys. Rev.* B **35** 482
[9] Blaha P, Schwarz K, Madsen G K H, Kvasnicka D and Luitz J 2001 WEIN 2K: *An Aujmented Plane Wave + Local Orbitals* (Vienna University of Technology)
[10] Ambrosch-Draxl C and Sofo J O 2006 *Comput. Phys. Commun.* **175** 1
[11] Werner W S M, Glantschnig K and Ambrosch-Draxl C 2009 *J. Phys. Chem. Ref. Data* **38** 1013
[12] Kwei C M, Chen Y F, Tung C J and Wang J P 1993 *Surf. Sci.* **293** 202
[13] Ding Z-J and Shimizu R 1989 *Surf. Sci.* **222** 313
[14] Tanuma S, Powell C J and Penn D R 2011 *Surf. Interface Anal.* **43** 689
[15] Sorini A P, Kas J J, Rehr J J, Prange M P and Levine Z H 2008 *Phys. Rev.* B **74** 165111
[16] Denton C D, Abril I, Garcia-Molina R, Moreno-Marin J C and Heredia-Avalos S 2008 *Surf. Interface Anal.* **40** 1481
[17] Abril I, Garcia-Molina R, Denton C D, Perez-Perez F J and Arista N R 1998 *Phys. Rev.* A **58** 357
[18] Bourke J D and Chantler C T 2012 *J. Phys. Chem. A* **116** 3202
[19] Smith D Y and Shiles E 1978 *Phys. Rev.* B **17** 4689
[20] Palik E D 1998 *Handbook of Optical Constants of Solids III* (New York: Academic)
[21] Chantler C T and Bourke J D 2014 *J. Phys. Chem.* A **118** 909
[22] Chantler C T and Bourke J D 2010 *J. Phys. Chem. Lett.* **1** 2422

[23] Joly Y 2001 *Phys. Rev.* B **63** 125120
[24] Joly Y, Cabaret D, Renevier H and Natoli C R 1999 *Phys. Rev. Lett.* **82** 2398
[25] Hedin L and Lundqvist B I 1971 *J. Phys. C: Solid State Phys.* **4** 2064
[26] Chantler C T 1995 *J. Phys. Chem. Ref. Data* **24** 71
[27] Chantler C T 2000 *J. Phys. Chem. Ref. Data* **29** 597
[28] Scofield J H 1973 *Lawrence Livermore National Laboratory Report UCRL-51326*
[29] Kas J J, Rehr J J, Glover J L, and Chantler C T 2010 *Nucl. Instrum. Meth. Phys. Res.* A **619** 28
[30] Nagy I and Echenique P M 2012 *Phys. Rev.* B **85** 115131
[31] Caliebe W A, Soininen J A, Shirley E L, Kao C C and Hämäläinen K 2000 *Phys. Rev. Lett.* **84** 3907